Photoinitiated unimolecular decomposition of NO_2: Rotational dependence of the dissociation rate

I. Bezel, P. Ionov,[a] and C. Wittig[b]
Department of Chemistry, University of Southern California, Los Angeles, California 90089

(Received 21 June 1999; accepted 1 September 1999)

Photoinitiated unimolecular decomposition rate constants of rotationally excited NO_2 molecules have been measured near dissociation threshold (D_0) by employing a double resonance technique. Rotational selectivity has been achieved by using narrow-linewidth ($0.015\ cm^{-1}$) infrared excitation to prepare specific rotational levels ($N'=1,3,...,15$, $K_a'=0$) of the (1,0,1) vibrational level. The picosecond-resolution pump–probe technique has then been used to photodissociate the molecules thus tagged and to monitor the appearance of the NO product. Data have been obtained for two progressions of average excess energies, $\langle E\rangle - D_0$: (i) $10\ cm^{-1}+E_{101}^{rot}$ and (ii) $75\ cm^{-1}+E_{101}^{rot}$, where $\langle E\rangle$ denotes an average over the pump laser linewidth and E_{101}^{rot} is the rotational energy of the (1,0,1) $\tilde{X}\,^2A_1$ intermediate vibrational level. The measured rate constants do not display any noticeable dependence on N', which is a reflection of significant rovibronic interaction. Spin–rotation interaction, which has been implicated as the main source of rovibronic coupling for small values of N', is not likely to yield such a result. A model is proposed to describe the influence of rotation on the dissociation rate. The experimental data are consistent with a Coriolis coupling mechanism causing transitions to occur between K_a levels. © *1999 American Institute of Physics.* [S0021-9606(99)01744-4]

I. INTRODUCTION

There are numerous scientific benchmark systems that people return to—as pilgrims to Mecca—seeking knowledge and testing their comprehension of the world around them. They include hydrogen in quantum physics, *drosophila* (fruit fly) DNA in genetics, and the value of π in arithmetic. For gas phase physical chemistry, NO_2 could be such a system. Its importance to fundamental chemical processes has spawned extensive scrutiny for decades, and strong optical absorption in a convenient wavelength region has enabled spectroscopists to generate and analyze a vast amount of data. It has a sparse enough density of vibronic states to resolve them independently, yet sufficiently strong intramolecular interactions to lead to chaotic dynamics. The large amount of experimental data on NO_2 makes it an ideal test ground for examining theoretical methods and models. Since it is relatively simple, precise computer simulations can be carried out; yet it is too complex for these simulations to succeed completely.

In this paper, a specific issue concerning NO_2 unimolecular decomposition near the dissociation threshold ($D_0 = 25{,}128.57 \pm 0.05\ cm^{-1}$)[1] is addressed, namely, how the dissociation rate constant is affected by parent rotation. Excitation energies near D_0 are chosen because in this region the rotational energy comprises a significant fraction of the excess energy and therefore the effect of rotation is expected to be prominent.

Much work has been done on the photodissociation quantum yield at different temperatures[2] and it has been shown that dissociation can occur when the photon energy is less than D_0 as a consequence of molecular rotation.[3] Thus, rotational energy is available for dissociation. Also, the average dissociation rate constant as a function of photon energy has been measured for expansion cooled (i.e., almost non-rotating) molecules[4–8] and has been found to be smaller than for room temperature samples.[5,9,10] Though such experiments demonstrate unequivocally that rotational energy, on average, increases the dissociation rate constant, state-specific information cannot be gleaned.

The near-threshold dissociation of NO_2 occurs on the ground $\tilde{X}\,^2A_1$ potential energy surface (PES) via a barrierless pathway which leads to $NO(X\,^2\Pi_{1/2,3/2}) + O(^3P_{2,1,0})$.[11–15] In the energy range of interest in the present study (i.e., less then $120\ cm^{-1}$ above D_0) only the ground vibrational state of $NO(X\,^2\Pi_{1/2})$ and the lowest oxygen spin–orbit state ($^3P_2$) are accessible.

Photoexcitation of NO_2 is easy: strong absorption starting at $\sim 10\,000\ cm^{-1}$ is due to the low-lying $\tilde{A}\,^2B_2$ electronic state. Two other nearby electronic states (i.e., $\tilde{B}\,^2B_1$ and $\tilde{C}\,^2A_2$) are not optically accessible from the ground PES and also have much smaller densities of states at the energies of interest than does the ground PES.[11,16–23] The $\tilde{X}\,^2A_1$ and $\tilde{A}\,^2B_2$ electronic states are strongly coupled through the asymmetric stretch vibration and are completely mixed above $17\,000\ cm^{-1}$, giving rise to vibronic manifolds of A_1 and B_2 symmetries.[16,23] These manifolds are coupled to one another by rovibronic interactions, leading to rovibronic chaos above $23\,000\ cm^{-1}$.[17] Above the dissociation thresh-

[a]Current address: Applied Materials, Inc., 3320 Scott Avenue, Santa Clara, CA 95054.
[b]Author to whom correspondence should be addressed. Electronic mail: wittig@cheml.usc.edu

old, however, the mixing of different zeroth-order rovibronic states competes with decomposition. Consequently, the extent of rotationally induced energy transfer in this regime is not *a priori* clear.

Rovibrational and rovibronic interactions in NO_2 have been studied from the bottom of the ground PES to excitation energies near D_0.[16,17,23–29] Delon *et al.* have estimated the strengths of rovibronic interactions by using anticrossing experiments with strong magnetic fields,[25] as well as from statistical analyses of absorption spectra for rotationally cold molecules.[17] In both cases it was deduced that second order spin–orbit interaction is the main coupling mechanism. Another mechanism which is known to couple different rotational states is perpendicular Coriolis interaction.[27,28] Since NO_2 is a nearly prolate top, a symmetric top basis of rotational eigenfunctions is generally adopted:[17,24,25,30]

$$|N,K_a,\Gamma\rangle = \frac{1}{\sqrt{2}}(|N,K_a\rangle \pm |N,-K_a\rangle), \tag{1}$$

where N is the rotational quantum number, K_a is the projection of the rotational angular momentum onto the molecular a axis, and Γ is the symmetry of the rotational function.

Little is known about intramolecular coupling mechanisms above dissociation threshold, and a study of the rotational dependence of the dissociation rate constant can help to establish their respective contributions. It is not the goal of this paper to calculate absolute values of dissociation rate constants of rotating NO_2. What is pursued is how the dissociation rate constants change with rotation and which mechanisms participate. Thus, we are relieved of the necessity to predict the rate itself—it has been measured—and we can concentrate on the *variation* of the rate due to subtle rovibrational dynamics.

Most, if not all, of the mechanisms responsible for rovibronic couplings are known, though their respective importance in dissociating molecules is unclear. Moreover, experiments have been limited to either small angular momenta[3–8,16,17,24,25,31–34] or high rotational temperatures.[2,5,9] In the latter, the data are averaged over a number of rotational states. In the former, only the first one or two rotational states are observed, which makes extrapolation of the measured dependencies to higher rotational states ambiguous. In the present work, systematic measurements have been carried out on a progression of rotational states which spans approximately 100 cm^{-1} of rotational energy. Other systems in which unimolecular decomposition has been examined with rotational resolution are HFCO,[35] HCO,[36] CH_3O,[37] and CH_2CO,[38] and HOCl.[39,40]

In the present work, dissociation rate constants have been measured by using the picosecond-resolution pump–probe technique. The difference between this and earlier work from our group[5,8] is that in the present study single rotational levels are selected by using double resonance, as indicated in Fig. 1.

Measurements have been carried out for two progressions of the average energies $\langle E\rangle$: $D_0 + 10\,cm^{-1} + BN'(N'+1)$ and $D_0 + 75\,cm^{-1} + BN'(N'+1)$, where B is an NO_2 rotational constant, N' is the rotational quantum number at the (1,0,1) intermediate vibrational level, and the brackets denote an average over the linewidth of the picosecond pump pulse. The first excitation progression, with the average picosecond pump photon energy set to excite the rotationless system to energies just above D_0 (i.e., 10 cm^{-1}), was expected to be especially sensitive to the direction of energy transfer from vibrational to rotational degrees of freedom. The second excitation progression, set at the bottom of a ''step'' in the variation of the reaction rate constant versus energy,[5] was expected to be sensitive to the reverse direction of energy transfer, i.e., from rotation to vibration. The N' quantum number was varied from 1 to 15, which corresponds to (1,0,1) rotational energies up to 100 cm^{-1}. The dissociation rate constant was found to be unchanged. Were 100 cm^{-1} put into vibrational degrees of freedom, the rate constant would have increased by a factor of approximately two.[5] Clearly, rotation affects the dissociation dynamics a subtle way.

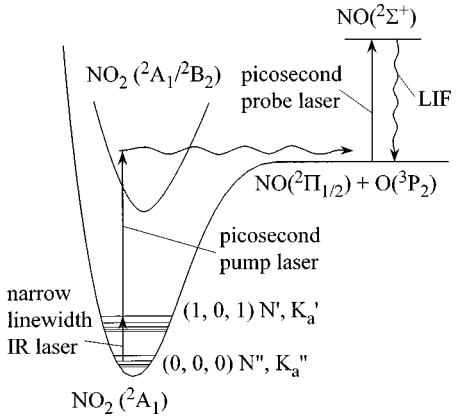

FIG. 1. Schematic of the double resonance experiment. Rotational selectivity is achieved by using a narrow-linewidth nanosecond IR laser. Following IR excitation, a picosecond pump pulse excites the ''tagged'' molecules to energies above the dissociation threshold. After a set delay, a picosecond probe pulse measures the amount of NO product via LIF. Only molecules which have absorbed both the IR and picosecond pump photons have enough energy to dissociate.

II. EXPERIMENT

The experimental arrangement is shown schematically in Fig. 2. It is noteworthy that over 10 mJ of 3.4 μm radiation was used in the first excitation step. This radiation derived from an optical parametric oscillator/amplifier system (OPO/OPA, STI Mirage 3000) pumped by an injection seeded Nd:YAG laser (Continuum NY81C or Powerlite 9000). Modifications to the Mirage 3000 enabled us to obtain 5–10 times more energy near 3.4 μm than is specified in the manual. These modifications include (i) increasing the beam size after the oscillator to match the aperture of the first amplifier, (ii) using a single pass first amplifier stage (instead of a resonant cavity) with corresponding adjustment of pump beam delay, (iii) increasing the lengths of the KTP crystals in the second amplifier stage from 15 to 20 mm, and (iv) careful compensation of divergence and astigmatism of the pump and seed beams. A color glass filter (Kopp 7-69) was added between the oscillator and the first amplifier to eliminate 1.7 μm radiation, which could cause interference in the first am-

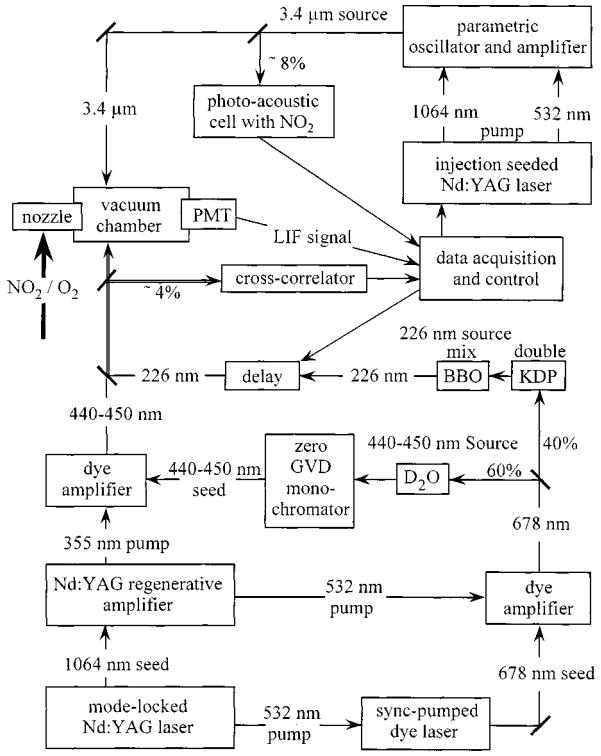

FIG. 2. Diagram showing the experimental arrangement.

plifier. A frequency stabilization system (Laser Vision) was used in some experiments to eliminate long term frequency drift.

About 8% of the 3.4 μm beam traversed an opto-acoustical cell containing ~1 Torr of room temperature NO_2. The opto-acoustical signal was monitored to ensure a correct excitation frequency. The linewidth at 3.4 μm is estimated to be approximately 0.015 cm^{-1}, based on resolution of the rotational transitions $13\leftarrow12$, $K_a=0$ and $13\leftarrow12$, $K_a=1$ of the $(1,0,1)\leftarrow(0,0,0)$ band, which are 0.04 cm^{-1} apart.[24] Table I lists the transitions used for the first excitation step.

Much of the present technique for generating short pump and probe pulses has been reported previously.[5,41,42] The primary source of subpicosecond pulses is a dual-jet mode-locked dye laser (Coherent 702-1) synchronously pumped by 2 W of second harmonic from an actively mode-locked Nd:YAG laser (Spectron SL 903). The Nd:YAG laser was driven at 76 MHz by a mode locked (CAMAC ML 4000).

TABLE I. Transitions used in the experiments; frequencies and assignments from Ref. 24.

N'	N''	K_a	$h\nu/cm^{-1}$	Other transitions within laser linewidth
1	2	0	2904.37	$15\leftarrow15$, $K_a=2$
3	2	0	2908.54	
5	4	0	2910.13	$8\leftarrow7$, $K_a=4$
7	6	0	2911.68	$10\leftarrow9$, $K_a=4$; $14\leftarrow13$, $K_a=6$; $20\leftarrow19$, $K_a=8$
9	8	0	2913.19	$19\leftarrow18$, $K_a=7$; $14\leftarrow13$, $K_a=5$
11	10	0	2914.64	$11\leftarrow10$, $K_a=1$
13	12	0	2916.06	
15	14	0	2917.43	$26\leftarrow25$, $K_a=7$

DCM special laser dye with DTDCI saturable absorber and a single-plate birefringent filter as a tuning element was used in the dye laser to obtain a train of 2 nJ~600 fs pulses at 678 nm. Pulses were selected at 10 Hz and amplified to ~2 mJ in a three stage ''red'' dye amplifier. Concentrations of the dye LDS 698 in MeOH in the different amplifier stages were chosen to optimize beam quality and energy. A Schott glass filter (RG780) was used as a solid state saturable absorber between the first and second amplifier stages to reduce amplified spontaneous emission (ASE) and pulse broadening.

Approximately 40% of the 2 mJ 678 nm pulses was tripled by using two 100 μm BBO crystals. This yielded a probe pulse with ~2 μJ of 226 nm radiation in a beam of ~3 mm diameter. The probe energy could be reduced by a half-wave plate before the doubling stage.

To form the pump pulse the remaining 60% of the 2 mJ 678 nm pulses was focused into a cell containing D_2O to produce a continuum, out of which a ~30 cm^{-1} width was selected by using a zero dispersion monochromator. A two stage ''blue'' amplifier was used to bring the energy up to 100 μJ with a beam diameter of ~6 mm. Coumarins 440 and 450 were used for 440 and 450 nm, respectively. To minimize ASE and improve the beam quality, a telescope with a pinhole in the focal plane and an interference filter were placed between the first and the second amplifier stages. The ''red'' and ''blue'' amplifiers were pumped by ~35 mJ of 532 nm and ~45 mJ of 355 nm (~80 ps pulses) from the regenerative amplifier (Quantel International RGA60) seeded with a fraction of the 1064 nm output of the Spectron SL903.

Pump and probe wavelengths and linewidths were measured with a double spectrometer (Spex 1401, 1800 grooves/mm, 0.15 cm^{-1} resolution), calibrated against a wavemeter (Burleigh WA-4500, accuracy ±1 cm^{-1}) by using the tunable output of a distributed feedback dye laser set at 22 222.5 cm^{-1}. This method enabled better absolute frequency calibration than in our preliminary report.[43,44] The uncertainty of the average pump photon energy of ±10 cm^{-1} is due to calibration, measurement of the spectrum, and frequency drift during the scan. The pump linewidth was ~30 cm^{-1} FWHM with a smooth close-to-Gaussian shape, while the probe was ~50 cm^{-1} FWHM, which was enough to cover the main band of the NO absorption spectrum.

After the probe beam encountered a computer controlled delay stage (Aerotech ATS100) the probe and pump pulses were combined collinearly by using a dichroic mirror. The beams were then focused into a vacuum chamber. A 30 cm focal length (f.l.) lens yielded the best signal/background ratio (see below). The sizes of the pump and probe beams on the lens were chosen to ensure that the probe was inside the pump focal volume. The 3.4 μm pulse was counter-propagating and arrived at the chamber ~50 ns before the pump and probe pulses. The best signal was obtained with a 35 cm f.l. lens for the 3.4 μm pulse. All three beams intersected ~1 mm from the nozzle orifice. LIF from NO was collected, filtered, detected with a photomultiplier, preamplified (Stanford Research fast preamplified SR445), digitized (Transiac 2001 and CAMAC 6001), averaged, and sent to a computer. The integrated signal trace served as a measure of the relative number of NO molecules.

The amount of NO signal was recorded as a function of the pump–probe delay. The entire delay range was 33.2 ps for all scans. Since some of the processes leading to NO background were pump–probe delay dependent (see below), data were recorded with the IR beam alternately on and off. Precautions were taken to avoid long-term drift of the lasers: after each 10 laser shots with the IR alternately on and off the delay stage was moved to the next point, such that it took only ~5 minutes to complete a scan over all delay points. After that the direction of the delay stage travel was reversed and the next scan was recorded. All IR-off scans were added together and subtracted from the sum of the IR-on scans; data handling details are given in Sec. III. A typical session lasted 2–4 hours and consisted of 100–200 measurements with the IR on and off for each pump–probe delay; the result of the session will be referred to hereafter as a ''scan.'' During a ''day'' of measurements, 3–6 4 hour scans were recorded, each with a different IR transition. Approximately eight scans were taken for each set of parameters. Typical scans are shown in Fig. 3.

The cross correlation between the pump and the probe pulses was recorded simultaneously with the LIF signal/background scan. To measure the cross correlation, ~4% of both the pump and the probe was split by a quartz window and focused into a 100 μm BBO crystal tuned to generate the difference frequency (DF). The DF wavelength was close to that of the ASE of the ''blue'' amplifier and the pump beam radiation, so the Spex 1401 spectrometer was used to select only a narrow (~0.5 cm^{-1}) spectral region of the DF. When recorded this way, the cross-correlation shape and position did not depend on the exact frequency, which is probably the consequence of negligible chirp in both the pump and the probe pulses. The cross-correlation signal from the photomultiplier was amplified and measured by a gated integrator and a boxcar averager.

NO_2 samples were prepared as follows: 1.5–2 atm of O_2 was sent through a bubbler containing NO_2 (Matheson 99.5%) at 0 °C. The resulting mixture (80–85% O_2 and 20–15% NO_2) was expanded into vacuum through a 0.2 mm pulsed (200 μs duration) nozzle. The O_2 pressure was optimized to provide the best signal for each rotational level. Precautions were taken to minimize NO_2 decomposition on metal surfaces: the delivery gas line was made of teflon and was pumped constantly in order to provide a fresh mixture to the nozzle orifice. These measures significantly reduced NO background.

The presence of a strong LIF background from NO was a serious obstacle. This background originated partially from NO in the molecular beam. However, using oxygen as the carrier gas and the nozzle modifications described above minimized background to the point where signals could be recorded. Another part of the background was due to photoinduced processes: though one 450 nm photon is not energetic enough to dissociate NO_2 from the ground state, two photon absorption brings NO_2 far above the dissociation threshold. In addition, 226 nm photons photodissociate NO_2. Another significant contribution to the background was due to the pump pulse: two-photon excitation of NO or three-photon excitation of NO_2. A precise assignment has not been made, but it is a fact that some of the backgrounds are pump–probe delay dependent and must be subtracted from the signal. Figure 4 shows a typical background trace. Since the processes contributing to the signal and to the background have different intensity dependencies, the intensities of the pump and probe pulses were adjusted to optimize the signal/background ratio. Even then, typical signal/background ratios were often <3.

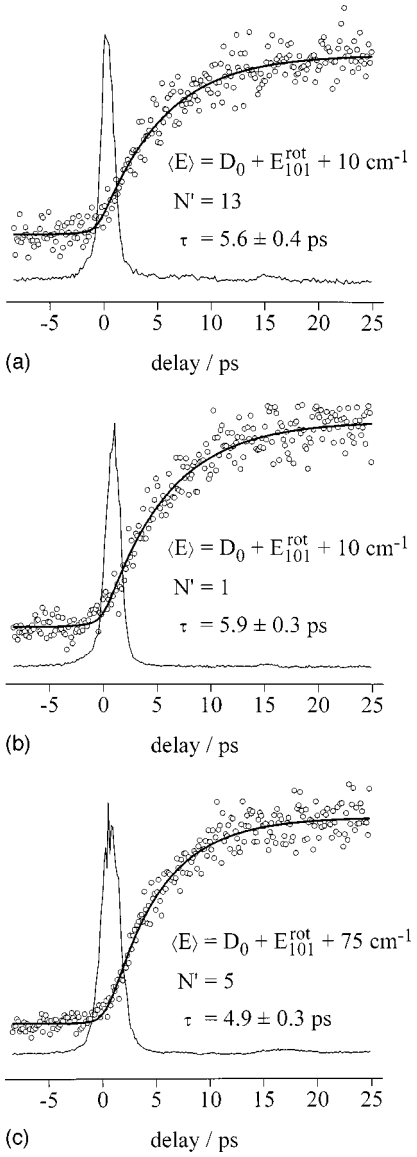

FIG. 3. (a)–(c) Typical signal and cross correlation scans for different excitation conditions. Circles: experimental product buildup traces (i.e., difference signals); thin lines: experimental cross correlations; thick lines: Eq. (8) is used to fit the buildup traces.

III. RESULTS

Data were obtained for two values of the average pump photon energy $\langle h\nu_{\text{pump}}\rangle$: 22,233 and 22 298 cm^{-1}. The corresponding average excitation energies $\langle E\rangle$ are given by

$$\langle E\rangle = E_{101}^{\text{vib}} + E_{101}^{\text{rot}} + \langle h\nu_{\text{pump}}\rangle, \tag{2}$$

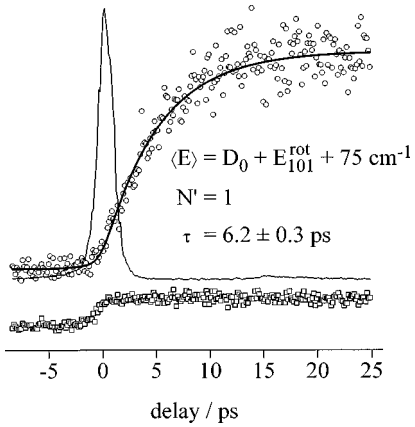

FIG. 4. Example of the ''background'' signal. Squares show the background recorded with the IR off. Other notations are the same as in Fig. 3. Note the time dependence of the IR-off signal.

where E_{101}^{vib} and E_{101}^{rot} are the vibrational and rotational energies, respectively, of the (1,0,1) intermediate vibrational level. Using $E_{101}^{\mathrm{vib}}=2906\,\mathrm{cm}^{-1}$, $D_0=25\,129\,\mathrm{cm}^{-1}$, and the values of $\langle h\nu_{\mathrm{pump}}\rangle$ given above yields

$$\langle E\rangle = D_0 + 10\ \ \mathrm{cm}^{-1} + E_{101}^{\mathrm{rot}} \tag{3}$$

and

$$\langle E\rangle = D_0 + 75\ \ \mathrm{cm}^{-1} + E_{101}^{\mathrm{rot}}. \tag{4}$$

Approximately eight scans were recorded for each set of $\langle h\nu_{\mathrm{pump}}\rangle$ and E_{101}^{rot} values, and each scan yielded a parameter which we designated as ''the rate constant.'' These rate constants were obtained as follows.

NO LIF signals were recorded with the IR beam alternately off and on at different delay times, resulting in $\overline{S_{\mathrm{off}}(t)}$ and $\overline{S_{\mathrm{on}}(t)}$, respectively, where the bar signifies an average over laser shots. Subtracting the former from the latter yielded the difference signal function, $S(t)$. Standard deviations were calculated at each pump–probe delay, t_i, by using

$$\sigma(t_i)^2=\sigma_{\mathrm{on}}(t_i)^2+\sigma_{\mathrm{off}}(t_i)^2, \tag{5}$$

where $\sigma(t_i)$ is the standard deviation of the average at time t_i. $\sigma_{\mathrm{on}}(t_i)^2$ is given by

$$\sigma_{\mathrm{on}}(t_i)^2=\frac{\overline{S_{\mathrm{on}}(t_i)^2}-\overline{S_{\mathrm{on}}(t_i)}^2}{N-1}, \tag{6}$$

where $\overline{S_{\mathrm{on}}(t_i)^2}$ is the average of the squared IR-on signal at t_i, $\overline{S_{\mathrm{on}}(t_i)}^2$ is the square of the average IR-on signal at t_i, and N is the number of laser shots at t_i (typically 100–200). The expression for $\sigma_{\mathrm{off}}(t_i)^2$ is also given by Eq. (6); i.e., the word *on* is replaced by the word *off*. The experimental scan, $S(t)$, was fitted to a single exponential buildup convoluted with the measured cross correlation by minimizing the χ^2 parameter:

$$\chi^2=\sum_{i=1}^{M}\frac{(S(t_i)-S_{\mathrm{fit}}(t_i))^2}{\sigma(t_i)^2}, \tag{7}$$

where M is the number of delay points and $S_{\mathrm{fit}}(t_i)$ is given by

$$S_{\mathrm{fit}}(t_i)=S_{\mathrm{baseline}}+A\int_{-\infty}^{t_i-t_0}dt'\ CC(t')\times\{1-\exp[-(t_i-t_0-t')/\tau]\}, \tag{8}$$

where t_0 is an offset for the delay between the signal and cross correlation traces, A and τ are the amplitude and buildup time parameters, respectively, $CC(t')$ is the experimental cross correlation curve, and S_{baseline} is the signal baseline. The cross correlation baseline was set at the average of the values measured at large negative and large positive delays. The adjustable parameters are A, S_{baseline}, t_0, and τ.

Since product buildup was assigned a single exponential, the use of a Levenberg–Marquardt fitting routine[45] was facilitated by using analytical derivatives, i.e., $\partial(\chi^2)/\partial p_i$ and $\partial^2(\chi^2)/\partial p_i\partial p_j$, where p_i and p_j denote the fit parameters. The experimental traces were fit and standard deviations for the τ values were calculated. Confidence levels for individual traces were used as weights for calculating the average τ values given in Table II.

The τ values listed in Table II indicate clearly a dependence on $\langle h\nu_{\mathrm{pump}}\rangle$. However, there is no significant dependence on the IR photon frequency, i.e., on E_{101}^{rot}. This is the major experimental finding of this work.

IV. DISCUSSION

A. The meaning of the experimental rates

Considerable theoretical work has been devoted to unimolecular reactions of polyatomic molecules. For example, a typical effective Hamiltonian approach treats a dissociating molecule as a system of discrete levels coupled to product continua, leading to resonance widths $\hbar\Gamma$.[46] Isolated resonances decay with single exponential rates Γ_i, whose average value, $\langle\Gamma_i\rangle$, is the conventional unimolecular decomposition rate constant k. Unfortunately, in most cases, the resonances overlap, making the situation more complicated.[47–52]

The NO_2 absorption spectrum does not display isolated transitions even a few wave numbers above D_0.[4,7,33,34] Though attempts have been made to extract dissociation rate constants from the spectral features observed in the threshold regime, there is no trust-worthy basis for doing so because of severe spectral congestion,[4,7,53,54] and therefore time resolved

TABLE II. Buildup times (τ) and standard deviations (σ) for different intermediate rotational levels (N'). The two values of $\langle h\nu_{\mathrm{pump}}\rangle$ correspond to progressions beginning at average excess energies of 10 and 75 cm^{-1}, as indicated in the headings.

		10 cm^{-1}		75 cm^{-1}	
N'	$E_{101}^{\mathrm{rot}}/\mathrm{cm}^{-1}$	τ/ps	σ/ps	τ/ps	σ/ps
1	1	5.8	0.2	5.1	0.3
3	5	6.5	0.3	5.0	0.4
5	13	6.3	0.4	4.6	0.2
7	24	6.2	0.5	4.9	0.2
9	38	6.1	0.3	4.9	0.3
11	56	6.5	0.3	4.7	0.3
13	77	5.7	0.2	4.7	0.2
15	101	6.0	0.3	4.1	0.3

measurements are needed for determining rate constants with good accuracy. In the regime of overlapping resonances, even the concept of resonances is somewhat abstract, since it is no longer possible to observe them individually, no longer possible to excite a single zeroth-order molecular eigenstate, and decay is no longer described by a single exponential. Moreover, in our experiments, NO_2 is excited by a spectrally broad laser pulse and therefore a number of zeroth-order vibronic states with different decay rates are accessed. Hence, the resulting kinetics are inherently nonexponential.

Abel *et al.* have monitored NO_2 survival versus time following excitation with a broad linewidth femtosecond pulse and have noted a nonexponential survival probability.[4] This was due in large part to the fact that a significant fraction of the molecules were excited to energies below D_0. When monitoring product buildup, neither the experiments of Ionov *et al.*[5] nor those discussed herein were able to discern nonexponential character. It should be emphasized that since NO product is monitored, the measurements are insensitive to NO_2 molecules which are excited to energies below D_0 or which dissociate very slowly.

To examine the sensitivity of our experiment to nonexponential product buildup, let us assume that the signal $S(t)$, is a sum of contributions, each having a rate constant k_i:

$$S(t)=\sum_i P_i\{1-\exp(-k_i t)\}, \tag{9}$$

where P_i is the probability of having the rate constant k_i. To examine modest ranges of k_i, $S(t)$ is expanded around the average value of the k_i, i.e.,

$$\langle k\rangle=\sum_i P_i k_i. \tag{10}$$

This yields

$$S(t)=\sum_i P_i-\exp\{-\langle k\rangle t\}\sum_i P_i(1+\Delta k_i t+\tfrac{1}{2}(\Delta k_i)^2 t^2+\cdots)$$

$$=1-(1+\tfrac{1}{2}\sigma^2 t^2+\cdots)\exp\{-\langle k\rangle t\}, \tag{11}$$

where $\Delta k_i=k_i-\langle k\rangle$ and $\sigma^2=\Sigma_i P_i(\Delta k_i)^2$ is the square of the variance.

To be observed, deviations from single exponential decay must exceed the noise level, which is ~10% in the present case. This results in $\sigma\sim 10^{11}\,s^{-1}$. In addition, the signal due to product buildup is a convolution of the molecular response function with the pump-probe cross correlation, whose temporal width is comparable to the dissociation times. This couples the fit parameters. Thus, to see deviations from single exponential buildup, a higher signal-to-noise ratio (S/N) is required than could be achieved in the present study. With the present S/N, we estimate (from numerical simulations) that to observe nonexponential behavior requires $\sigma\geqslant 4\times 10^{11}\,s^{-1}$, which is larger than the average rate constant itself.

Figure 5 illustrates some of the above considerations. A trace was generated by convoluting a 1.5 ps FWHM Gaussian cross correlation with two exponential buildups ($k_1=10^{11}\,s^{-1}$ and $k_2=3\times 10^{11}\,s^{-1}$) of equal weight ($P_1=P_2=0.5$, $\sigma=10^{11}\,s^{-1}$). The resulting trace was fit to a single exponential buildup by using the same routine as with the experimental traces, but with a 1.5 ps FWHM Gaussian as $CC(t)$ in Eq. (8), and with all $\sigma(t_i)=1$ in Eq. (7). The best fit was obtained with $\tau^{-1}=1.8\times 10^{11}\,s^{-1}$, which is only 10% smaller than the average decay rate constant. The traces are barely distinguishable.

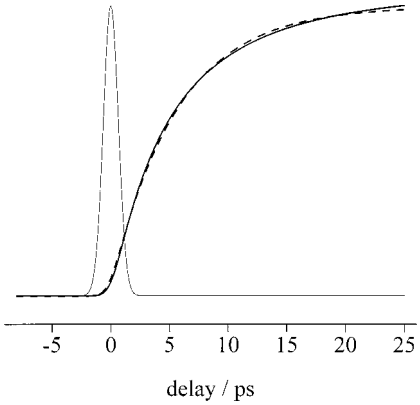

FIG. 5. Fitting a two-exponential buildup with a single exponential. The solid line is the function $(1-0.5e^{-0.1t}-0.5e^{-0.3t})$ convoluted with a 1.5 ps FWHM Gaussian cross correlation (thin line); time (t) is in picoseconds. The dashed line is the fit given by Eq. (8). The traces are barely distinguishable.

The same procedure was used to obtain rate constants for the different unimolecular decomposition models discussed below. Namely, product buildup was calculated and convoluted with a 1.5 ps FWHM Gaussian cross correlation, and the resulting trace was fit to a single exponential by using Eq. (8) with a Gaussian $CC(t)$.

The dissociation rate constants determined in our experiments are close to the average rate constants given by Eq. (10). From random matrix analyses of the survival probability, it has been argued that the decay of a system in the regime of strongly overlapping resonances might be slower than a single-exponential function with the parameter $\langle k\rangle$.[47,49,55] However, in using the (calculated) data of Ref. 45 when product buildup is fit by using a single exponential the same way as with our experimental data, the fit gives the average rate constant to within ~5%.

Despite the fact that our measurements are not very sensitive to the spread of the contributing rates, the average rate constant can be determined with good accuracy. We estimate that ⩾30% variation of an average rate constant would be detectable.

B. Influence of molecular rotation on the dissociation rate

The microcanonical unimolecular decomposition rate constant can be expressed as[56,57]

$$k(E)=\frac{W^{\ddagger}(E)}{h\rho(E)}, \tag{12}$$

where ‡ denotes the transition state (TS), E is the total energy relative to the zero-point level of the parent, $W^{\ddagger}(E)$ is the number of open channels at the TS, $\rho(E)$ is the reactant

density of states, and h is Planck's constant. It is obvious, yet significant, that uncertainties in $k(E)$ accrue from uncertainties in both $W^{\ddagger}(E)$ and $\rho(E)$. For nonrotating molecules on a single PES, $\rho(E)$ is the vibrational density of states, and when two or more PES's are strongly coupled, $\rho(E)$ is the corresponding vibronic density of states. When symmetry is present, both $W^{\ddagger}(E)$ and $\rho(E)$ should be sorted according to symmetry species.

At energies below D_0, it is possible to obtain $\rho(E)$ spectroscopically, for example, by counting the number of levels accessed in an absorption spectrum. However, above D_0, $\rho(E)$ cannot be obtained spectroscopically, since absorption spectra are congested—even in the first few cm^{-1} above D_0 with samples cooled to a few K.[4,7,33,34] Consequently, $\rho(E)$ must be either calculated or obtained by extrapolation from below D_0.[12,14,16,22]

The dramatic increase of $\rho(E)$ observed near D_0 (Refs. 1, 4, 7, 32, 58, and 62) casts doubt on the viability of extrapolations in the immediate vicinity of D_0. In addition, $W^{\ddagger}(E)$ generally cannot be measured, necessitating accurate electronic structure and dynamics calculations, and parent rotation and nonzero electronic spin further complicate matters. Even state-of-the-art calculations of $W^{\ddagger}(E)$ and $\rho(E)$ cannot reproduce near-threshold effects.[12,13,59–61]

The above limitations notwithstanding, the energy dependence of Eq. (12) can assist in the determination of how the dissociation rate constant changes with parent rotation. Namely, though $W^{\ddagger}(E)$ and $\rho(E)$ cannot be measured separately, $k(E)$ for rotationally cold NO_2 [hereafter referred to as $k_{\mathrm{nonrot}}(E)$, see Fig. 6] has been measured[5] and will be used as an empirical input to the model presented below; the pathological region within the first few wave numbers near D_0 (Refs. 1, 4, 7, 32, 58, and 62) will be neglected.

For rotating polyatomic molecules, only the total angular momentum and its projection on a laboratory-fixed axis have good quantum numbers, i.e., J and M_J, respectively. Effects due to nuclear spin can be neglected on the timescale of the present studies. The rotational angular momentum and its projection on a molecule-fixed axis [with the corresponding (prolate) symmetric top quantum number K_a] are not rigorously conserved. That is, states with different N and K_a can be coupled through rovibronic interactions.

Molecular rotation can influence the dissociation dynamics via several mechanisms. Let us distinguish two types: (i) those that do not change the rotational state of the molecule, such as centrifugal distortion of the potential and parallel Coriolis interaction; and (ii) those that couple different rotational states (while of course conserving total angular momentum, including its projection on a laboratory fixed axis) and destroy vibronic symmetry, such as perpendicular Coriolis and spin–rotation interactions.

Centrifugal distortion of the potential is too small to alter the vibronic density of states significantly. However, the energy associated with centrifugal distortion may be of the same order of magnitude as the energy available at the TS, and therefore the number of open channels can be affected significantly. If the rotational state is unchanged throughout the course of reaction, Eq. (12) can be written[56,57]

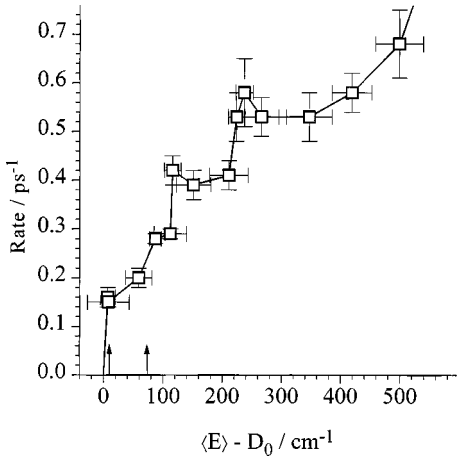

FIG. 6. Dissociation rate constants of rotationally cold molecules. Squares denote experimental values (Ref. 4). Horizontal error bars indicate the excitation linewidths; vertical error bars are standard deviations. The two arrows show the onsets of the double resonance progressions. The solid lines are the linear interpolation used to obtain $k_{\mathrm{nonrot}}(E)$.

$$k_{\mathrm{nomix}}(E)=\frac{W^{\ddagger}(E-E^{\ddagger}_{\mathrm{rot}})}{h\rho(E)}=k_{\mathrm{nonrot}}(E-E^{\ddagger}_{\mathrm{rot}}), \tag{13}$$

where E is the total energy including parent rotation, $E^{\ddagger}_{\mathrm{rot}}$ is the rotational energy of the molecule at the TS, and $\rho(E)$ is assumed to be constant throughout the modest range of E values studied here. For NO_2, both $W^{\ddagger}(E-E^{\ddagger}_{\mathrm{rot}})$ and $\rho(E)$ are symmetry-sorted according to vibronic species. Equation (13) implies that rotation and vibration can be separated at the TS and that the number of open channels depends only on the excess energy $E-E^{\ddagger}_{\mathrm{rot}}$.

$E^{\ddagger}_{\mathrm{rot}}$ depends on the TS geometry through the rotational constants $A^{\ddagger}$, $B^{\ddagger}$, and $C^{\ddagger}$, and the quantum numbers N, K_a (prolate limit), and K_c (oblate limit). For the present modeling, the TS is taken to be at $R=3$ Å and $\theta=130°$ in Jacobi coordinates.[11,28,59] The influence of the TS geometry will be discussed below. In the present case, $B^{\ddagger}$ and $C^{\ddagger}$ are close enough to justify the symmetric top approximation:

$$E^{\ddagger}_{\mathrm{rot}}(N,K_a)=B^{\ddagger}N(N+1)+(A^{\ddagger}-B^{\ddagger})K_a^2, \tag{14}$$

which should be substituted into Eq. (13) to obtain $k_{\mathrm{nomix}}(E)$. A linear interpolation to data measured at 6 K[5] is used to obtain $k_{\mathrm{nonrot}}(E-E^{\ddagger}_{\mathrm{rot}})$, as shown in Fig. 6.

Now consider the situation in which rotational states with different K_a values are coupled by rovibronic interaction. For the sake of simplicity electron spin is neglected in this section, in which case N is a good quantum number. Equation (12) is premised on an ergodic assumption: all zeroth-order states are thoroughly mixed and the corresponding classical motion is chaotic. Analyses of NO_2 absorption spectra in the range of a few thousands of wave numbers below D_0 show that the K_a quantum number breaks down, leading to so-called rovibronic chaos.[1,7,17,62] However, above the reaction threshold, randomization of the K_a quantum number competes with dissociation, and therefore the extent of K_a mixing is not *a priori* clear.

Complete K_a mixing prior to dissociation gives

$$k_{\text{fullmix}}(N,E)=\sum_{K_a=0}^{N}\frac{W^{\ddagger}(E-E^{\ddagger}_{\text{rot}}(N,K_a))}{(N+1)h\rho(E)}$$

$$=\frac{1}{N+1}\sum_{K_a=0}^{N}k_{\text{nonrot}}(E-E^{\ddagger}_{\text{rot}}(N,K_a)), \quad (15)$$

where level countings for $W^{\ddagger}$ and $\rho(E)$ are carried out over vibronic levels. The $N+1$ term accounts for the increase of the density of available states due to $N+1$ projections of the rotational angular momentum on the molecular axis. Note that $N+1$ is used, rather than the $2N+1$ possible states that arise from projecting the rotational angular momentum on the molecular axis. This is due to the fact that most of the vibronic levels in the vicinity of D_0 have either A_1 or B_2 symmetry.[16,22,23] Of the levels above D_0 which have $K_a=0$, even N, and A_1 total symmetry (following double-resonance excitation), only half of the states can be mixed efficiently, i.e., those with A_1 or B_2 rotational symmetry. Those of B_1 or A_2 rotational symmetry require B_1 or A_2 vibronic wave functions, respectively, which can only arise from $\tilde{B}\,^2B_1$ and $\tilde{C}\,^2A_2$ electronic states. However, since the $\tilde{B}\,^2B_1$ and $\tilde{C}\,^2A_2$ vibronic manifolds have much smaller densities of states, they are neglected.

To simulate the data, product buildup was calculated by using the selection rules for the $\tilde{A}\,^2B_2\leftarrow\tilde{X}\,^2A_1$ parallel transition. Namely, suppose the initially prepared rotational state of the (1, 0, 1) vibrational level has quantum numbers N' and $K_a'=0$. The photoexcited dissociative levels then have quantum numbers $N=N'\pm1$ and $K_a=0$, with the photoexcitation probabilities proportional to the Hönl–London factors:

$$\frac{(N'+1)^2}{(N'+1)(2N'+1)} \quad \text{and} \quad \frac{N'^2}{(N'+1)(2N'+1)} \quad (16)$$

for the R and P branch transitions, respectively.[63] The contributions from the P and R branch transitions were averaged accordingly.

Figure 7 shows the results of such simulations for two extreme cases: (a) no K_a mixing, and (b) complete K_a mixing. Obviously, these limiting cases are not able to reconcile the data. With no K_a mixing, the rate constant increases with N over the range $1\leqslant N\leqslant 15$, whereas for complete K_a mixing, the rate constant decreases with N. Mixing of different N via spin–rotation coupling does not change this. The above dependencies are intuitive: if $K_a=0$ is preserved, the rate constant increases because the energy available for reaction increases with N. On the other hand, for complete K_a mixing, the rate constant decreases because the high-K_a zeroth-order rovibronic states accessed via energy transfer dissociate slowly (or even not at all) when K_a is sufficiently large.

At zero rotation the calculated rate constants do not coincide exactly with those obtained in the double resonance experiments. However, this does not signify a discrepancy between the double resonance results and the one-photon measurements. The dissociation rate constants in the double resonance experiments—extrapolated to zero rotation—are 1.6×10^{11} and $2.0\times10^{11}\,\text{s}^{-1}$ for $\langle E\rangle-D_0=10$ and 75 cm^{-1}, respectively. The one-photon results for expansion cooled samples (where effects due to rotational excitation are minimal) yields the same rate constants for $\langle E\rangle-D_0=8$ and 59 cm^{-1}, respectively, i.e., at approximately the same energies.[5] The difference can be attributed to the linear interpolation used for $k_{\text{nonrot}}(E)$, which smoothes any structure in the variation of the reaction rate constant with energy.

The only parameter in the model which is not determined experimentally is the TS geometry. The ground PES, on which dissociation occurs, is barrierless, resulting in TS's at large separations for nonrotating molecules just above threshold. Grebenshchikov *et al.* have studied TS positions

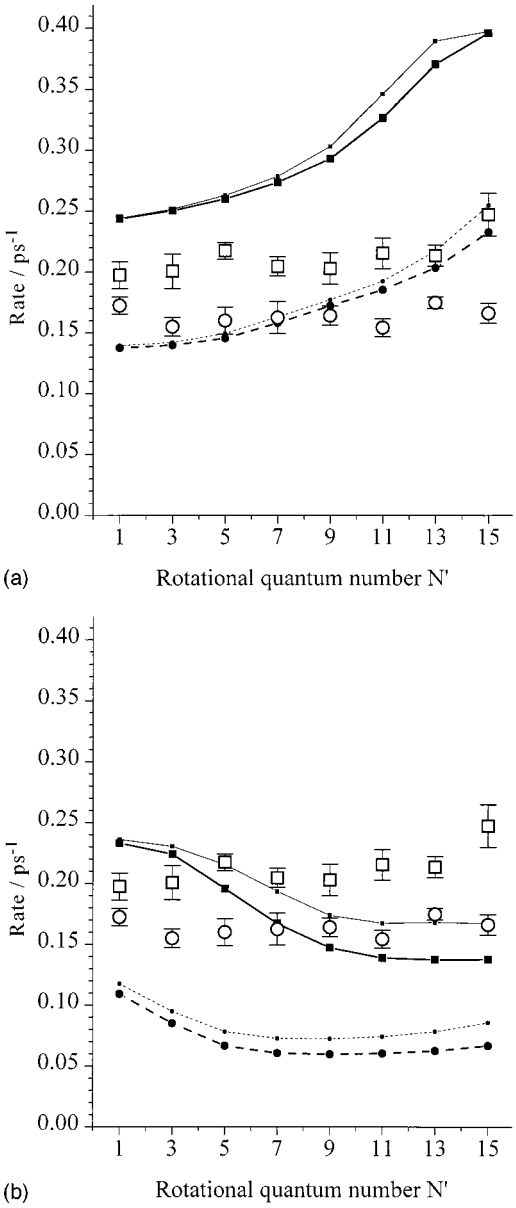

FIG. 7. Comparison of simulated and experimental dissociation rate constants. Circles and dashed lines are for $\langle E\rangle-D_0=10\ \text{cm}^{-1}+E^{\text{rot}}_{101}$; squares and solid lines are for $\langle E\rangle-D_0=75\ \text{cm}^{-1}+E^{\text{rot}}_{101}$. Open symbols indicate experimental data; error bars indicate standard deviations. Lines indicate simulations: (a) no K_a mixing; (b) complete K_a mixing. Thick lines indicate a TS at $R=3$ Å and $\theta=130°$ (Jacobi coordinates) with rotational constants $A^{\ddagger}=3.02\ \text{cm}^{-1}$ and $B^{\ddagger}=0.166\ \text{cm}^{-1}$. Thin lines indicate a TS at $R=3.5$ Å and $\theta=120°$ with $A^{\ddagger}=2.3\ \text{cm}^{-1}$ and $B^{\ddagger}=0.125\ \text{cm}^{-1}$. These extreme cases do not fit the data.

by using classical trajectories. They found that as the excess energy increases to just a few tens of cm^{-1} the TS moves inward to separations of slightly more than 3 Å.[59] At yet higher energies, the variation of the TS position is modest. For example, it moves further inward by only ~0.1 Å for the next 1000 cm^{-1}. Similar results can also be obtained by analyzing the PES calculated earlier by Katagiri and Kato.[11] Namely, bending levels orthogonal to the reaction coordinate result in barriers at ~3 Å for excess energies of ~80 cm^{-1}. Klippenstein *et al.* also place the TS at ~3 Å.[12] Furthermore, NO_2 rotation facilitates tightening of the TS near threshold, since the binding energy at 3 Å is tens of cm^{-1}, i.e., comparable to the centrifugal barriers. Although the TS is thought to be at much larger separations right at D_0, there is no reliable model to describe quantitatively the TS tightening, and for the present calculations the TS was set at 3 Å regardless of excitation energy and angular momentum. Different TS geometries do not produce qualitatively different results, as shown in Fig. 7.

From the comparison given in Fig. 7, it is concluded that dissociation takes place in a regime of intermediate coupling. Namely, rotational levels other than $K_a=0$ participate, but the rotational dynamics are not fully ergodic on the dissociation time scale. To model such a regime, explicit values of the coupling matrix elements are needed.

C. Coriolis, spin–rotation, and inertial asymmetry coupling mechanisms

Coupling of different rotational states occurs via interactions such as Coriolis, spin–rotation, and inertial asymmetry. For NO_2 at energies near D_0, spin–orbit and Coriolis interactions are believed to be particularly important.[17,27,28,30]

1. Spin–rotation coupling

It has been shown by Bird *et al.* that spin–rotation coupling near the minimum of a potential well is dominated by a second-order interaction which involves spin–orbit and orbit–rotation terms.[67] Moreover, Delon *et al.* have deduced that for rotationally cold NO_2 the mixing of the zeroth-order rotational levels which occurs in the range 17 000–23 945 cm^{-1} is due primarily to this mechanism.[17,25] An expression for the relevant coupling matrix elements has been derived by Hallin and Merer:[30]

$$\begin{aligned}&\langle \eta_1,N_1,K_{a_1},S,J|H_{sr}|\eta_2,N_2,K_{a_2},S,J\rangle\\&=(-1)^{N_2+S+J}\sqrt{S(S+1)(2S+1)(2N_1+1)(2N_2+1)}\\&\times\begin{Bmatrix}J & S & N_1\\ 1 & N_2 & S\end{Bmatrix}(-1)^{N_1-K_{a_1}}\sum_q\begin{pmatrix}N_1 & 1 & N_2\\ -K_{a_1} & q & K_{a_2}\end{pmatrix}\\&\times\langle \eta_1\|T_q^1(\text{vibronic})\|\eta_2\rangle,\end{aligned}\tag{17}$$

where J is the total angular momentum excluding nuclear spin, S is the electronic spin, $\langle \eta_1\|T_q^1(\text{vibronic})\|\eta_2\rangle$ is the reduced matrix element for the vibronic part of the interaction, which depends only on the vibronic states $|\eta_1\rangle$ and $|\eta_2\rangle$, and the curly brackets and big parentheses denote 6-j and 3-j symbols, respectively. Delon *et al.* have found that the average value of the magnitude of the reduced matrix element:

$$V_0^{\text{sr}}=\overline{|\langle A_1\|T_1^1(\text{vibronic})\|B_2\rangle|}\tag{18}$$

is $0.7\pm0.1\,cm^{-1}$ near D_0.[17] They pointed out that the $q=0$ term in Eq. (17) (i.e., corresponding to $\Delta N=\pm1$, $\Delta K_a=0$) can be neglected, since it couples the A_1 and B_2 vibronic states to the relatively sparse B_1 and A_2 vibronic manifolds. The surviving coupling terms have $q=\pm1$, for which $\Delta N=0,\pm1$, $\Delta K_a=\pm1$. Referring to Eq. (17), for values of $S=1/2$, $K_{a_1}=K_a$, and $K_{a_2}=K_a+1$, the only surviving term in the summation is that with $q=1$, and Eq. (17) becomes

$$\begin{aligned}&\overline{|\langle \eta_1,N_1,K_a,S,J|H_{sr}|\eta_2,N_2,K_a+1,S,J\rangle|}\\&=\sqrt{\tfrac{3}{2}(2N_1+1)(2N_2+1)}\begin{Bmatrix}J & \frac{1}{2} & N_1\\ 1 & N_2 & \frac{1}{2}\end{Bmatrix}\\&\times\begin{pmatrix}N_1 & 1 & N_2\\ -K_a & 1 & K_a+1\end{pmatrix}V_0^{\text{sr}}.\end{aligned}\tag{19}$$

This expression can be used to see how the H_{sr} matrix elements scale with the rotational quantum numbers. In fact, they are approximately constant with respect to N and K_a. This is not obvious from the equation, but follows from the explicit values of the 6-j and 3-j symbols.

2. Coriolis coupling

Grebenshchikov *et al.* have used classical trajectory calculations to demonstrate that the robustness of the K_a quantum number decreases with increasing NO_2 rotational excitation due to perpendicular Coriolis and inertial asymmetry couplings.[28] The off-diagonal Coriolis matrix elements are given by[30]

$$\begin{aligned}&\langle \eta_1,N,K_a|H_{\text{Cor}}|\eta_2,N,K_a\pm1\rangle\\&=-\sqrt{N(N+1)-K_a(K_a\pm1)}\langle \eta_1\|BL_B\mp CL_C\|\eta_2\rangle,\end{aligned}\tag{20}$$

where A, B, and C are rotational constants and L_B and L_C are components of the orbital angular momentum operator. The S and J quantum numbers are conserved and therefore omitted from the notation. Upon introducing the average magnitude of the reduced Coriolis matrix element:

$$V_0^{\text{Cor}}=\overline{|\langle A_1\|BL_B\mp CL_C\|B_2\rangle|},\tag{21}$$

where A_1 and B_2 denote the coupled vibronic species, the average magnitude of the matrix element given in Eq. (20) can be written as

$$\overline{|\langle \eta_1,N,K_a|H_{\text{Cor}}|\eta_2,N,K_a\pm1\rangle|}=\sqrt{N(N+1)-K_a(K_a\pm1)}V_0^{\text{Cor}}.\tag{22}$$

The spin–rotation and Coriolis matrix elements have very different dependencies on the rotational quantum numbers. Namely, the matrix elements given by Eq. (22) grow almost linearly with increasing N (for low K_a), while the matrix elements given by Eq. (19) stay approximately constant with increasing N.

3. Inertial asymmetry coupling

Off-diagonal matrix elements due to inertial asymmetry also have a significant dependence on the rotational quantum numbers. This mechanism couples rotational states according to $\Delta N=0$, $\Delta K_a=\pm 2$. For a nearly prolate top, in the first approximation:[64]

$$\langle \eta,N,K_a|H_{\text{asym}}|\eta,N,K_a\pm 2\rangle=\tfrac{1}{4}(\overline{C}-\overline{B})\sqrt{(N(N+1)-K_a(K_a\pm 1))(N(N+1)-(K_a\pm 1)(K_a\pm))}, \tag{23}$$

where $\overline{B}$ and $\overline{C}$ are vibrationally averaged rotational constants. For low K_a, the matrix elements grow approximately quadratically with N.

Because of the N dependencies of their off-diagonal matrix elements, Coriolis and asymmetry couplings can both take place to a significant extent in the present experiments, even though their roles are believed to be secondary relative to that of spin–rotation coupling at low N.[17,25] For fast rotation, asymmetry and/or Coriolis couplings are significant even for modest values of their reduced matrix elements.

There is an important difference between these two mechanisms. Inertial asymmetry coupling comes about because an asymmetric top Hamiltonian is approximated by a symmetric top Hamiltonian. Thus, the perturbation does not operate on the electronic and vibrational parts of the wave function. The asymmetry couples different zeroth-order symmetric top rotational wave functions built on the same electronic/vibrational state.[65,66] On the other hand, Coriolis coupling arises from motion in a rotating reference frame, and therefore can couple different vibronic states.

The inertial asymmetry of NO_2 is not large. At the bottom of the ground PES the A, B, and C rotational constants are 7.99, 0.43, and 0.41 cm^{-1}, respectively.[67] The B and C values change slightly with vibration, whereas A is sensitive to bending. Regardless, the molecule remains close to a symmetric top. For example, for the (1,0,1) vibrational level, A, B, and C are 7.85, 0.43, and 0.405 cm^{-1},[24] while for (2,13,1), they are 16.0, 0.43, and 0.41 cm^{-1}.[27] Highly vibrationally excited molecules may become either more or less symmetric than the ground state, depending on the shape of the PES.

Rotational constants near D_0 have not been measured, but estimates from trajectory calculations suggest that $|\overline{B}-\overline{C}|$ is only 0.013 cm^{-1}.[68] With this amount of inertial asymmetry, and given the large separations between K_a levels, we conclude that the effects of asymmetry can be neglected in the present study.

D. K_a mixing in competition with unimolecular decomposition

A model is presented here in which vibronic levels having particular N and K_a values dissociate, with rate constants given by Eq. (13), in competition with K_a mixing (Fig. 8). The following phenomenological equations are used to describe this competition:

$$\frac{dP_{N,K_a}(E,t)}{dt}=-k_{N,K_a}P_{N,K_a}(E,t)-\sum_{\tilde{N}}\sum_{\tilde{K}_a=0}^{\tilde{N}}\gamma_{N,K_a;\tilde{N},\tilde{K}_a}(P_{N,K_a}(E,t)-P_{\tilde{N},\tilde{K}_a}(E,t)), \tag{24}$$

where $P_{N,K_a}(E,t)$ is the population at energy E and time t of levels having N and K_a quantum numbers, $\gamma_{N,K_a;\tilde{N},\tilde{K}_a}$ is the mixing rate constant between (N,K_a) and $(\tilde{N},\tilde{K}_a)$, and N and $\tilde{N}$ can assume the values $J\pm 1/2$. The dissociation rate constants k_{N,K_a} are given by

$$k_{N,K_a}=k_{\text{nonrot}}(E-E^{\ddagger}_{\text{rot}}(N,K_a)) \tag{25}$$

with $E^{\ddagger}_{\text{rot}}(N,K_a)$ given by Eq. (14).

The set of Eqs. (24) was solved by using a fourth-order Runge–Kutta routine with initial populations obtained by using the optical selection rules and the Hönl–London factors given by Eq. (16). Product buildup at energy E was calculated by using

$$P_{\text{prod}}(E,t)=\sum_{N}\sum_{K_a=0}^{N}(P_{N,K_a}(E,0)-P_{N,K_a}(E,t)) \tag{26}$$

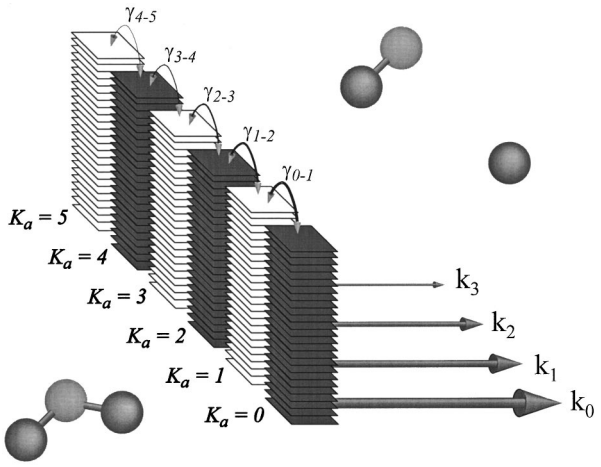

FIG. 8. Schematic representation of the couplings. The stacks represent zeroth-order rovibronic manifolds of A_1 (dark) and B_2 (light) vibronic symmetry, sorted according to rotational quantum numbers. Each stack can either dissociate with a rate given by Eq. (13) or undergo transitions to other stacks with rates given by Eq. (28). Arrow thicknesses indicate qualitative trends.

and $P_{\mathrm{prod}}(E,t)$ was then averaged over the 30 cm^{-1} FWHM Gaussian model excitation line shape, $g(E)$:

$$P(t)=\frac{\int_{D_0}^{\infty} dE\, g(E) P_{\mathrm{prod}}(E,t)}{\int_{D_0}^{\infty} dE\, g(E)}. \tag{27}$$

To obtain the total product buildup, $P(t)$ traces for four transitions (i.e., $J=N\pm 1/2$, $N=N'\pm 1$, and $\Delta K_a=0$) were summed. The result was convoluted with the 1.5 ps FWHM Gaussian model cross correlation and then it was fit to a single exponential [Eq. (8)] to obtain the parameter τ, which is compared to the experimental result.

In the model, the initially prepared $K_a=0$ levels couple to other K_a levels via successive $\Delta K_a=\pm 1$ couplings. Recall that our qualitative conclusion concerning the degree of K_a mixing is that a significant fraction of the K_a phase space is mixed prior to dissociation. Consequently, since the measured dissociation rates are equal to or exceed $1.6\times 10^{11}\,\mathrm{s}^{-1}$, the rate constants $\gamma_{N,K_a;\tilde{N},\tilde{K}_a}$ must be at least comparable to this.

In the strong coupling limit (i.e., $V_\rho \gg 1$, where V is the coupling matrix element) the K_a mixing rate constants are given by Fermi's golden rule:

$$\gamma_{N,K_a;\tilde{N},\tilde{K}_a}=\frac{2\pi}{\hbar}V^2\rho. \tag{28}$$

In this regime, $\gamma_{N,K_a;\tilde{N},\tilde{K}_a}$ is proportional to V^2 as long as ρ is independent of rotation. For a given coupling mechanism, i.e., one whose matrix elements scale as per Eqs. (19) or (22), the $\gamma_{N,K_a;\tilde{N},\tilde{K}_a}$ were varied to attain the best fit to the data.

As mentioned above, though the vibronic density of states above D_0 is not known, extrapolation from energies below D_0 (but avoiding the pathological region just a few cm^{-1} below D_0) gives $\sim 0.38/\mathrm{cm}^{-1}$ for each symmetry species.[16] In the following discussion, the relation between the average coupling matrix elements and the transition rate constant is assumed to be given by Eq. (28) with $\rho=0.38/\mathrm{cm}^{-1}$, even though $V_\rho \gg 1$ is not satisfied for small values of the matrix elements. A slightly better approximation is given by the picket fence model of Bixon and Jortner:[69]

$$\gamma_{N,K_a;\tilde{N},\tilde{K}_a}=\frac{2}{\hbar}\sqrt{V^2+(\pi V^2\rho)^2}. \tag{29}$$

However, using Eq. (29) in place of Eq. (28), with V given by any of Eq. (19) or (22), does not change the results. Equation (29) differs from Fermi's golden rule for small V, i.e., small coupling rate constants. However, for small coupling rate constants, contributions from K_a values other than zero are negligible. Thus, using Eq. (28) only results in an underestimation of the effect of the smallest coupling matrix elements. Results that use Eq. (29) are given by thin lines in Figs. 9 and 10. Traces corresponding to the same values of coupling matrix elements are almost identical.

Figure 9 shows rate constants which have been calculated by assuming that spin–rotation interaction is the sole coupling mechanism. If V_0^{sr} is taken to be 0.7 cm^{-1} [Fig. 9(a)], as measured by Delon *et al.*,[17,25] the simulated dependence is almost indistinguishable from that of no K_a mixing shown in Fig. 7(a). This can be understood in terms of the K_a changes which are needed for K_a mixing to cause measurable effects. For example, for high N, changing K_a from 0 to 1 or 2 has essentially no effect on the rate constant, as can be seen from Eqs. (13) and (14).

To bring the high-N rate constants down, the coupling matrix elements must be made an order of magnitude larger.

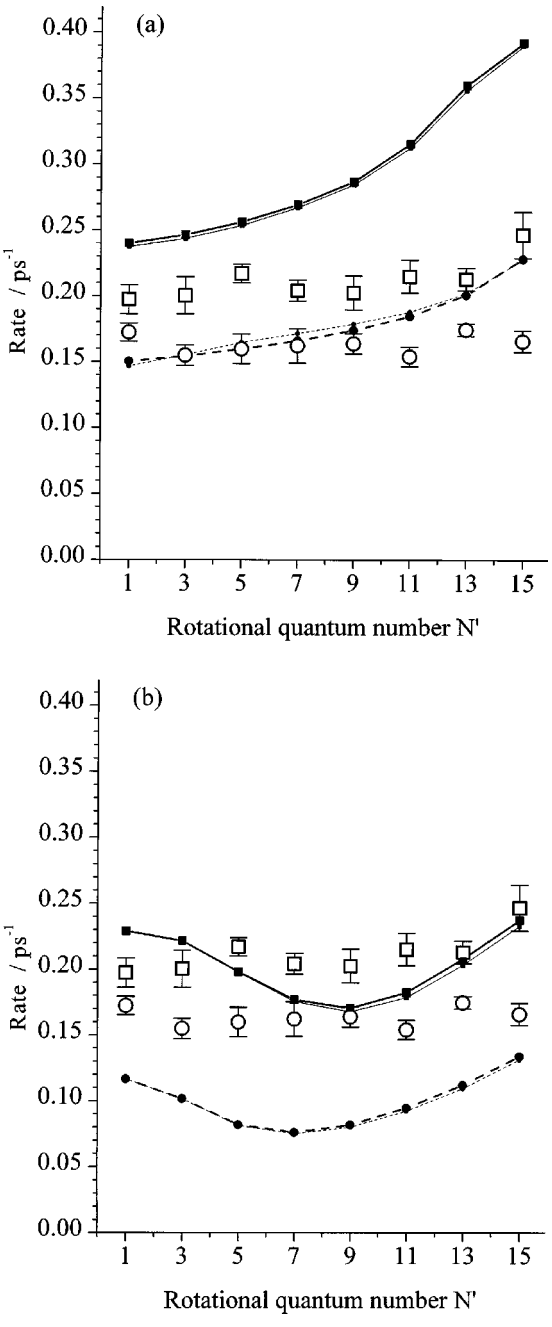

FIG. 9. Comparison of simulated and experimental dissociation rate constants. The simulations assume spin–rotation coupling only; see Eq. (19). Circles and dashed lines are for $\langle E\rangle - D_0 = 10\,\mathrm{cm}^{-1} + E_{101}^{\mathrm{rot}}$; squares and solid lines are for $\langle E\rangle - D_0 = 75\,\mathrm{cm}^{-1} + E_{101}^{\mathrm{rot}}$. Open symbols indicate experimental data; error bars indicate standard deviations. Thick lines are calculated using Eq. (28), i.e., Fermi's golden rule; thin lines are calculated using Eq. (29), i.e., the picket fence model of Bixon and Jortner. (a) $V_0^{\mathrm{sr}} = 0.7\,\mathrm{cm}^{-1}$; (b) $V_0^{\mathrm{sr}} = 10\,\mathrm{cm}^{-1}$.

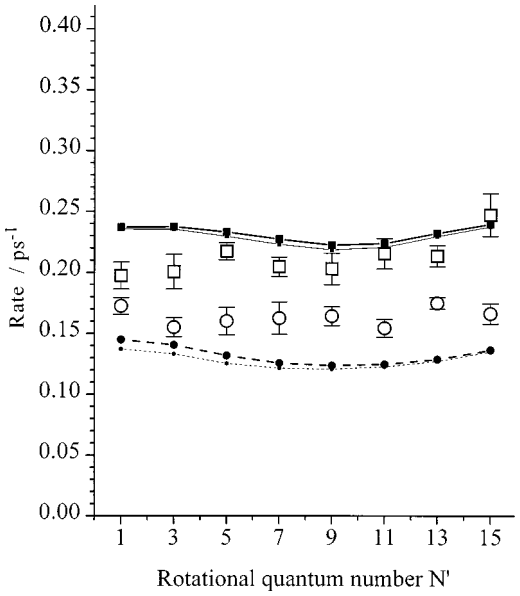

FIG. 10. Comparison of simulated and experimental dissociation rate constants. The simulations assume Coriolis coupling only [$V_0^{\mathrm{Cor}}=0.3\,\mathrm{cm}^{-1}$, see Eq. (22)]. Notations as in Fig. 8.

However, in this case, the rate constants at intermediate N values drop, as shown in Fig. 9(b). A broad range of coupling strengths has been examined, and the conclusion is that it is not possible to reconcile the data by using N-independent K_a mixing rate constants.

A significantly better fit to the data is obtained when it is assumed that Coriolis coupling dominates, as shown in Fig. 10. Good agreement is achieved by assuming that the average coupling rate constants between K_a and $K_a \pm 1$ are given by

$$[N(N+1)-K_a(K_a\pm 1)]\times 4\times 10^{10}\,\mathrm{s}^{-1} \tag{30}$$

which corresponds to $V_0^{\mathrm{Cor}}=0.3\,\mathrm{cm}^{-1}$. Recall that the relevant basis of comparison is the N' variation of the rates, rather than absolute values.

The N^2 scaling of the coupling rate constant for $\Delta K_a = \pm 1$ enables the calculated rates to fit the data. As mentioned above, the first-order term of the spin–rotation interaction expansion does not work, since there is almost no N dependence. Moreover, higher-order spin–rotation terms are believed to be significantly smaller.[17] Thus, we conclude that Coriolis coupling can reconcile the experimental results.

Our verdict about the significance of Coriolis coupling is supported by trajectory calculations which focus on Coriolis and inertial asymmetry couplings, ignoring electron spin.[59] This study shows that coupling between adjacent K_a levels increases approximately linearly with N, with almost one third of the available K_a phase space populated prior to dissociation, regardless of the speed of rotation. Though it is hard to extract the value of the average coupling matrix element from the trajectory study, further insight can be gained from spectroscopic studies which have been carried out below D_0.

Values for $\overline{|\langle 1,0|H_{\mathrm{Cor}}|1,1\rangle|}$ and $\overline{|\langle 3,0|H_{\mathrm{Cor}}|3,1\rangle|}$ can be obtained by using Eq. (22) with $V_0^{\mathrm{Cor}}=0.3\,\mathrm{cm}^{-1}$. This yields values of approximately 0.4 and 1.0 cm^{-1}, respectively. These values exceed the average rovibronic matrix element of 0.28 cm^{-1} which was obtained by analyzing absorption spectra for the same upper states in the region $\sim$1500 cm^{-1} below D_0.[17] If V_0^{Cor} were $\sim$0.3 cm^{-1} at energies below D_0, it should have been detected: (i) spectroscopically in the region 16 000–19 362 cm^{-1}, where Delon *et al.* report matrix elements of $\sim$0.2 cm^{-1} for both $|0,1\rangle$ and $|0,3\rangle$ rotational levels;[17] and (ii) in magnetic anticrossing experiments carried out near 17 700 cm^{-1}.[25]

This can be a manifestation of enhanced Coriolis coupling at energies near D_0, due to large amplitude vibrations. Alternatively, it can reflect an incorrect choice of the model parameters. The value of the Coriolis reduced matrix element obtained from the fit is a function of the TS geometry. For example, variation of the Jacobi angle of the TS from 120° to 140° results in a twofold increase of the $A^{\ddagger}$ rotational constant and a concomitant change of the Coriolis coupling strength required to rationalize the data. It would be imprudent to include more than one fitting parameter in the above model. However, when the magnitudes of the average coupling matrix elements are known, such a model can be used to predict dissociation rate constants of rotating molecules as well as $k(T)$, since the computational effort is minimal.

The constancy of the dissociation rate constant with increasing rotational excitation is due to a balance between (i) increasing the total energy available for reaction and (ii) including zeroth-order high-K_a states which are slowly dissociating and/or nondissociating in the photoexcited ensemble. The double resonance results are not in conflict with the observed rate constant increase for room temperature samples.[5,9] In the work reported here, K_a was always initially zero. However, if high-K_a levels were excited initially, K_a mixing would then increase the amount of energy available for dissociation and the rate constant would increase.

V. CONCLUSION

The variation of the NO_2 unimolecular decomposition rate constant with parent rotational excitation has been measured for two progressions of the average excess energies, $\langle E\rangle - D_0$: (i) $10\,\mathrm{cm}^{-1}+E_{101}^{\mathrm{rot}}$; and (ii) $75\,\mathrm{cm}^{-1}+E_{101}^{\mathrm{rot}}$, where E_{101}^{rot} is the rotational energy (with corresponding quantum numbers N' and K_a') of the (1,0,1) intermediate vibrational level. The double resonance technique, combined with the picosecond-resolution pump–probe technique, has enabled N' to be examined in the range $1 \leqslant N' \leqslant 15$ for $K_a'=0$, i.e., $0 \leqslant E_{101}^{\mathrm{rot}} \leqslant 100\,\mathrm{cm}^{-1}$. The addition of up to 100 cm^{-1} of rotational energy does not have a noticeable effect on the rate constant. This is interpreted as evidence for complex rovibrational dynamics.

A simple model has been used to calculate the dissociation rate constants for rotating molecules. Subject to the inherent limitations of the model, this exercise suggests that coupling between different rotational states increases with rotational excitation. A good fit is achieved when K_a couples to $K_a \pm 1$ with a rate constant that varies as $\sim N^2$. This coupling is attributed to perpendicular Coriolis interaction, with a reduced matrix element of $V_0^{\mathrm{Cor}} \leqslant 0.3\,\mathrm{cm}^{-1}$.

ACKNOWLEDGMENTS

This research was supported by a grant from the National Science Foundation. The authors have benefited greatly from discussions with S. Ionov, S. Grebenshchikov, K. Liu, and H. Reisler.

[1] R. Jost, J. Nygård, A. Pasinski, and A. Delon, J. Chem. Phys. **105**, 1287 (1996).
[2] C. M. Roehl, J. J. Orlando, G. S. Tyndall, R. E. Shetter, G. J. Vazquez, C. A. Cantrell, and J. G. Calvert, J. Phys. Chem. **98**, 7837 (1994).
[3] U. Robra, H. Zacharias, and K. H. Welge, Z. Phys. D **16**, 175 (1990).
[4] B. Abel, H. H. Hamann, and N. Lange, Faraday Discuss. **102**, 147 (1995).
[5] S. I. Ionov, G. A. Brucker, C. Jaques, Y. Chen, and C. Wittig, J. Chem. Phys. **99**, 3420 (1993).
[6] G. A. Brucker, S. I. Ionov, Y. Chen, and C. Wittig, Chem. Phys. Lett. **194**, 301 (1992).
[7] J. Miyawaki, K. Yamanouchi, and S. Tsuchiya, J. Chem. Phys. **99**, 254 (1993).
[8] I. Bezel, D. Stolyarov, and C. Wittig, J. Phys. Chem. **in press**, (1999).
[9] H. Gaedtke, H. Hippler, and J. Troe, Chem. Phys. Lett. **16**, 177 (1972).
[10] B. Abel, paper presented at ACS Meeting, Anaheim CA, 1999.
[11] H. Katagiri and S. Kato, J. Chem. Phys. **99**, 8805 (1993).
[12] S. J. Klippenstein and T. Radivoyevitch, J. Chem. Phys. **99**, 3644 (1993).
[13] D. M. Wardlaw and R. A. Marcus, J. Chem. Phys. **83**, 3462 (1985).
[14] J. Troe, Chem. Phys. **190**, 381 (1995).
[15] L. B. Harding, H. Stark, J. Troe, and V. G. Ushakov, Phys. Chem. Chem. Phys. **1**, 63 (1999).
[16] R. Georges, A. Delon, and R. Jost, J. Chem. Phys. **103**, 1732 (1995).
[17] A. Delon, R. Georges, and R. Jost, J. Chem. Phys. **103**, 7740 (1995).
[18] C. F. Jackels and E. R. Davidson, J. Chem. Phys. **64**, 2908 (1976).
[19] C. P. Blahous III, B. F. Yates, Y. Xie, and H. F. Schaefer III, J. Chem. Phys. **93**, 8105 (1990).
[20] G. D. Gillispie and A. U. Khan, J. Chem. Phys. **65**, 1624 (1976).
[21] C. F. Jackels and E. R. Davidson, J. Chem. Phys. **65**, 2941 (1976).
[22] B. M. Toselli and J. R. Barker, J. Phys. Chem. **93**, 6578 (1989).
[23] E. Haller, H. Köppel, and L. S. Cederbaum, J. Mol. Spectrosc. **111**, 377 (1985).
[24] V. Dana and J. P. Maillard, J. Mol. Spectrosc. **71**, 1 (1978).
[25] A. Delon, P. Dupre, and R. Jost, J. Chem. Phys. **99**, 9482 (1993).
[26] A. Delon, R. Jost, and M. Lombardi, J. Chem. Phys. **95**, 5701 (1991).
[27] A. Perrin, C. Camy-Peyret, and J.-M. Flaud, J. Mol. Spectrosc. **88**, 237 (1981).
[28] S. Y. Grebenshchikov, H. Flöthmann, R. Schinke, I. Bezel, C. Wittig, and S. Kato, Chem. Phys. Lett. **285**, 410 (1998).
[29] S. L. Coy, K. K. Lehmann, and F. C. DeLucia, J. Chem. Phys. **85**, 4297 (1988).
[30] K.-E. J. Hallin and A. J. Merer, J. Mol. Spectrosc. **65**, 163 (1977).
[31] A. Delon and R. Jost, J. Chem. Phys. **95**, 5686 (1991).
[32] J. Miyawaki, K. Yamanouchi, and S. Tsuchiya, J. Chem. Phys. **101**, 4505 (1994).
[33] T. J. Butenhoff and E. Rohlfing, J. Chem. Phys. **98**, 5460 (1993).
[34] T. J. Butenhoff and E. Rohlfing, J. Chem. Phys. **98**, 5469 (1993).
[35] Y. Choi and C. B. Moore, J. Chem. Phys. **97**, 1010 (1992).
[36] J. D. Tobiason, J. R. Dunlop, and E. A. Rohlfing, J. Chem. Phys. **103**, 1448 (1995).
[37] S. Dertinger, A. Geers, J. Kappert, J. Wiebrecht, and F. Temps, Faraday Discuss. **102**, 31 (1995).
[38] A. Mellinger, M. V. Ashikhmin, and C. B. Moore, J. Chem. Phys. **108**, 8944 (1998).
[39] R. J. Barnes, G. Dutton, and A. Sinha, J. Phys. Chem. A **101**, 8374 (1997).
[40] R. J. Barnes and A. Sinha, J. Chem. Phys. **107**, 3730 (1997).
[41] S. I. Ionov, G. A. Brucker, C. Jaques, L. Valachovic, and C. Wittig, J. Chem. Phys. **97**, 9486 (1992).
[42] S. I. Ionov, G. A. Brucker, C. Jaques, L. Valachovic, and C. Wittig, J. Chem. Phys. **99**, 6553 (1993).
[43] P. I. Ionov, I. Bezel, S. I. Ionov, and C. Wittig, Chem. Phys. Lett. **272**, 257 (1997).
[44] The different excitation energy from the value reported in Ref. 43 is due to better calibration of the monochromator used to measure the excitation pulse spectrum. Previously, it was calibrated by using the nearest strong line of a mercury lamp (435–833 nm) which is $\sim$700 cm^{-1} to the blue of the region of interest. In the present work, it is calibrated against a wave meter (Burleigh WA-4500) using the tunable output of a DFDL laser set at 22 222.5 cm^{-1}.
[45] W. H. Press, S. A. Teukolsky, W. T. Vettering, and B. P. Flannery, *Numerical Recipes* (Cambridge University Press, Cambridge, UK, 1992).
[46] C. Cohen-Tannoudji, J. Dupont-Roc, and G. Grynberg, *Atom-Photon Interactions* (Wiley, New York, 1992).
[47] U. Peskin, H. Reisler, and W. H. Miller, J. Chem. Phys. **101**, 9672 (1994).
[48] U. Peskin and W. H. Miller, J. Chem. Phys. **102**, 8874 (1995).
[49] M. Desouter-Lecomte and F. Culot, J. Chem. Phys. **98**, 7819 (1993).
[50] T. A. Brody, J. Flores, J. B. French, P. A. Mello, A. Pandey, and S. S. M. Wong, Rev. Mod. Phys. **53**, 385 (1981).
[51] V. A. Mandelshtam, T. P. Grozdanov, and H. S. Taylor, J. Chem. Phys. **103**, 10074 (1995).
[52] M. L. Mehta, *Random Matrices* (Academic, San Diego, 1991).
[53] C. Wittig and S. I. Ionov, J. Chem. Phys. **100**, 4714 (1994).
[54] J. Miyawaki, K. Yamanouchi, and S. Tsuchiya, J. Chem. Phys. **100**, 4716 (1994).
[55] L. Zhu and W. L. Hase, Chem. Phys. Lett. **175**, 117 (1990).
[56] T. Baer and W. L. Hase, *Unimolecular Reaction Dynamics: Theory and Experiments* (Oxford University Press, New York, 1996).
[57] R. G. Gilbert and S. C. Smith, *Theory of Unimolecular and Recombination Reactions* (Blackwell Scientific Publications, Oxford, 1990).
[58] A. Delon, S. Heilliette, and R. Jost, Chem. Phys. **238**, 465 (1998).
[59] S. Y. Grebenshchikov, C. Beck, H. Flöthmann, R. Schinke, and S. Kato, J. Chem. Phys. **111**, 619 (1999).
[60] R. F. Salzgeber, V. A. Mandelshtam, C. Schlier, and H. S. Taylor, J. Chem. Phys. **110**, 3756 (1999).
[61] R. F. Salzgeber, V. A. Mandelshtam, C. Schlier, and H. S. Taylor, J. Chem. Phys. **109**, 937 (1999).
[62] S. I. Ionov, H. F. Davis, K. Mikhaylichenko, L. Valachovic, R. A. Beaudet, and C. Wittig, J. Chem. Phys. **101**, 4809 (1994).
[63] G. Herzberg, *Molecular Spectra and Molecular Structure* (Van Nostrand-Reinhold, New York, 1966).
[64] H. W. Kroto, *Molecular Rotation Spectra* (Dover, Mineola, 1992).
[65] E. B. Wilson and B. Howard, J. Chem. Phys. **4**, 260 (1936).
[66] E. B. Wilson, J. Chem. Phys. **4**, 313 (1936).
[67] G. R. Bird, J. C. Baird, A. W. Jache, J. A. Hodgeson, J. R. F. Curl, A. C. Kunkle, J. W. Bansford, J. Rastrup-Andersen, and J. Rosenthal, J. Chem. Phys. **40**, 3378 (1964).
[68] S. Y. Grebenshchikov (private communication).
[69] M. Bixon and J. Jortner, J. Chem. Phys. **48**, 715 (1968).